



Wiley Analytical Science

Virtual Conference

The 5th edition of the Wiley Analytical Science Conference starts November 8, 2022!

Featured Sessions:

- **Integration of X-ray microscopy and finite elements into a digital twin**

Thurs Nov 10, 10:00 - 10:30 AM EST / 4:00 - 4:30 PM CET

- **Optimization of Cryo TEM lamella preparation workflows to be faster and more accessible**

Wed Nov 16, 10:00 - 11:00 AM EST / 4:00 - 5:00 PM CET

events.bizzabo.com/WASconferenceFall2022



Seeing beyond



WILEY

Desolvation Synergy of Multiple H/Li-bonds on Iron–Dextran–based Catalyst Stimulates Lithium–Sulfur Cascade Catalysis

Tingting Li, Dong Cai, Shuo Yang*, Yangyang Dong, Shuang Yu, Ce Liang, Xuemei Zhou, Yongjie Ge, Kuikui Xiao, Huagui Nie, Zhi Yang**

T. Li, Dr. D. Cai, Dr. S. Yang, Y. Dong, S. Yu, C. Liang, Dr. X. Zhou, Dr. Y. Ge, Dr. K. Xiao, Prof. H. Nie, Prof. Z. Yang

Key Laboratory of Carbon Materials of Zhejiang Province, Wenzhou University, Wenzhou, 325035, China

E-mail: caidong@wzu.edu.cn; yangshuo@wzu.edu.cn; yang201079@126.com

Dr. S. Yang

College of Electrical and Electronic Engineering, Wenzhou University, Wenzhou, 325035, China

Keywords: lithium–sulfur battery; iron dextran; H/Li–bond; cascade catalysis; lithium polysulfide conversion

Traditional lithium–sulfur battery catalysts are still facing substantial challenges in solving sulfur redox reactions which involve multistep electron transfers and multiphase transformations. Here,

This article has been accepted for publication and undergone full peer review but has not been through the copyediting, typesetting, pagination and proofreading process, which may lead to differences between this version and the [Version of Record](https://onlinelibrary.wiley.com/doi/10.1002/adma.202207074). Please cite this article as [doi: 10.1002/adma.202207074](https://onlinelibrary.wiley.com/doi/10.1002/adma.202207074).

This article is protected by copyright. All rights reserved.

Accepted Article

inspired by the combination of iron dextran (INFeD) and ascorbic acid (VC) as a blood tonic for the treatment of anemia, we developed a highly efficient VC@INFeD catalyst in the sulfur cathode, accomplishing the desolvation and enrichment of high-concentration solvated lithium polysulfides at the cathode/electrolyte interface with the assistance of multiple H/Li-bonds and resolving subsequent sulfur transformations through gradient catalysis sites where the INFeD promotes long-chain lithium polysulfide conversions and VC accelerates short-chain lithium polysulfide conversions. Comprehensive characterizations reveal that the VC@INFeD can substantially reduce the energy barrier of each sulfur redox step, inhibit shuttle effects, and endow the lithium-sulfur battery with high sulfur utilization and superior cycling stability even under a high sulfur loading (5.2 mg cm^{-2}) and lean electrolyte (electrolyte/sulfur ratio, $\sim 7 \text{ } \mu\text{L mg}^{-1}$) condition.

1. Introduction

Rechargeable lithium-sulfur (Li-S) batteries have been reckoned as a powerful energy supplier for next-generation electronic devices due to the high theoretical energy density (2600 Wh kg^{-1}) and low cost ($\approx 0.25 \text{ } \$ \text{ kg}^{-1}$ for sulfur).^[1] Unfortunately, it suffers from notorious intermediate lithium polysulfide (LiPS, Li_2S_n , $2 < n \leq 8$) shuttling and sluggish multiphase sulfur redox reactions (SRR, solid S_8 -liquid LiPSs-solid $\text{Li}_2\text{S}_2/\text{Li}_2\text{S}$), which results in low cyclability and slow progress of the commercialization.^[2] In the past decades, scientists have mainly developed three strategies to conquer this issue: 1) physical adsorption or confinement of sulfur species by using carbon materials (e.g., graphene, carbon nanotubes (CNTs), hierarchically porous carbon); 2) chemical adsorption through organic/inorganic metal compounds (for example, metal oxides, metal sulfides, metal-

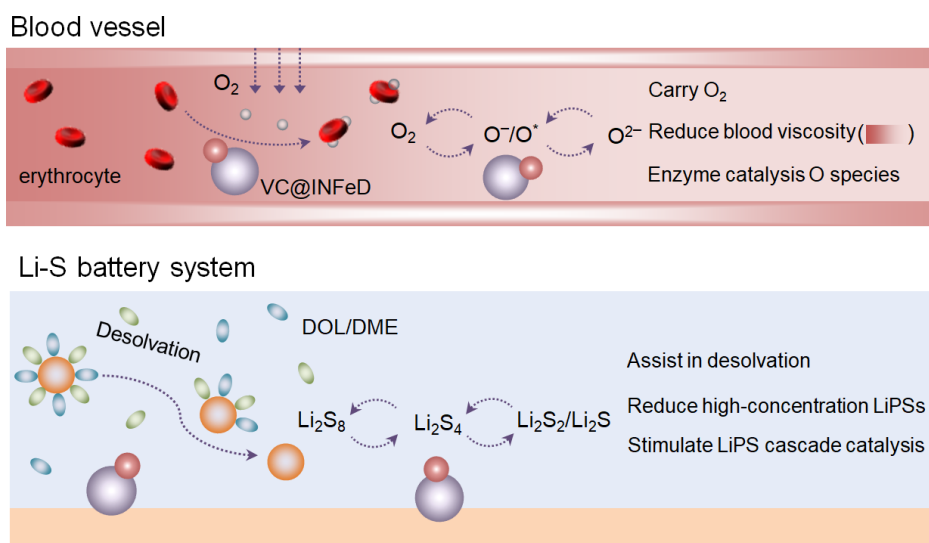
This article is protected by copyright. All rights reserved.

organic-frameworks);^[3] 3) designing catalytic systems for accelerating sulfur conversions. Despite great progress has been achieved by these strategies, the as-prepared Li-S batteries can hardly survive under high-sulfur loading and lean-electrolyte where high-concentration LiPSs cannot be efficiently and completely eliminated.

In Li-S chemistry, the sulfur conversion involves multi-step homogeneous/heterogeneous reactions with liquid-liquid, liquid-solid, solid-solid, and solid-liquid alternating interconnection transformations, and a slow but lengthy 16-electron transfer.^[4] Generally, an ideal catalyst for LiPS transformation is considered to be integrated with proper LiPS adsorption ability, superior conductivity, and catalytic ability; whereas, from the perspective of classical catalysis, an easy neglectful factor is the complex solvation/desolvation effects of ether-based solvents on LiPS conversions.^[5] Actually, LiPSs are initially surrounded by solvent molecules to form organic-inorganic clusters,^[6] *i.e.*, solvation structure; as the chain length gets shorter, the solubility of LiPSs decreases, and so does the number of solvent molecules on the surface,^[7] where the interaction strength depends largely on the bonds between Li⁺ of LiPSs and O atoms of 1,2-Dimethoxyethane (DME) or 1,3-dioxolane (DOL), namely Li...O bonds or Li-bonds.^[8] In addition, it was found that the mediation of solvent molecules could rebuild the catalyst surface and subsequently affect sulfur conversions, which is analogous to the numerous reports on H-bonds in aqueous batteries.^[9] Given the complexity of this catalytic system and the neglect of solvation effects in catalytic processes, conventional catalysts cannot realize their potential to convert high-concentration LiPSs. Therefore, it is crucial to search for appropriate catalysts that match current ether-based solvents for developing practical high-energy-density Li-S batteries.

This article is protected by copyright. All rights reserved.

Taking inspiration from nature,^[10] we found that hemoglobin is the porter of O₂ in human blood whose insufficiency will lead to symptoms of anemia and subsequently affect enzyme catalysis of oxygen reduction reactions (ORR).^[11] In pharmaceutical chemistry, iron dextran (INFeD) in conjunction with ascorbic acid (VC) has been recommended for the treatment of anemia, where hydroxyl-rich H-bonds of dextran chains can modulate solvated interactions and decrease blood viscosity; multivalent iron (Fe²⁺/Fe³⁺) centers are conducive to carrying and transforming O₂.^[12] More importantly, after being absorbed, it has a good blood-replenishing effect and can catalyze complicated ORR at the three-phase (catalyst/solvent/oxygen species) reaction interface under ambient temperature.^[13] According to the periodic expansion catalysis concept reported before,^[14] the clue of ORR catalyst design is a good reference for solving the SRR problems faced by Li-S batteries. If H-bond networks are rationally designed on the catalyst/electrolyte interface to cooperate with Li-bonds, the enrichment and transfer of solvated LiPSs on the catalyst surface can be realized, further stimulating subsequent catalytic processes (**Scheme 1**). This strategy to realize the regulation of the catalyst/electrolyte interface by drawing on the role of biological iron dextran has yet to be reported in the field of Li-S batteries.



Scheme 1. Schematic illustration of the inspiration for this VC@INFeD molecular catalyst design from pharmaceutical chemistry to Li-S chemistry.

Herein, we developed an efficient molecular VC@INFeD catalyst in Li-S cathode, which was composed of an INFeD polymer chain attached with VC and explored the structure-activity relationships and catalytic micro-mechanisms. Through systematically studying SRR, activation energies, in situ spectra, and electrochemical performances, it is found that the VC@INFeD can capture solvated LiPS clusters via H-bonds to form localized high-concentration LiPS distribution at the cathode/electrolyte interface and propel them to rapidly transfer and transform at gradient catalytic sites assisting by Li-bonds and Fe^{2+}/Fe^{3+} active centers where the INFeD has a good catalytic effect on long-chain LiPS conversion reactions; while the VC is more inclined to accelerate short-chain LiPS conversion reactions. As a result, the Li-S battery delivers promising electrochemical performance with high capacity and excellent rate capability even under high sulfur loading and lean

electrolyte conditions.

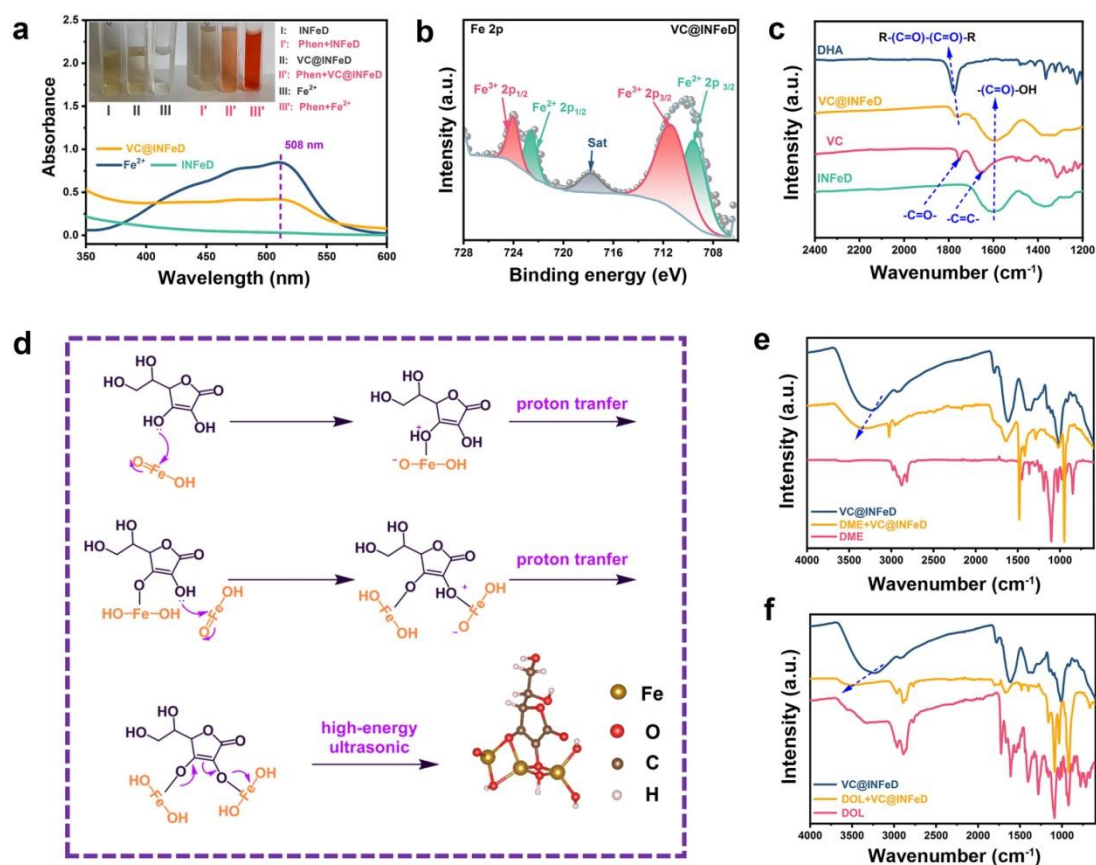
2. Results and Discussions

2.1. Synthesis and Characterization of VC@INFeD: As illustrated in Figure S1a (Supporting Information), INFeD which is composed of ferric hydroxide (FeOOH) core and dextran shell is a hollow and spherical particle with various diameters (~10 to 50 μm). When it is used as the reaction mediator in Li-S battery systems, the smooth surface and clear boundaries between particles would substantially hinder electron/ion transfer.^[15] To solve this problem, VC and carbon nanotubes (CNTs) were used to construct 3D conductive networks on the surface of INFeD (denoted as VC@INFeD) through a high-energy ultrasonic treatment. That is because VC can destroy the external-layered structure of INFeD (Figure S1b, Supporting Information) and thus CNTs can be tightly and evenly embedded on the generated surface, forming electron transport channels. In stark contrast, CNTs fail to attach on INFeD without the assistance of VC and tend to aggregate (Figure S2, Supporting Information).

Accordingly, the reaction mechanisms between INFeD and VC as well as the composition and configuration of VC@INFeD were further investigated. It was found that, by assisting strong reductive VC, Fe^{3+} of INFeD can be easily converted to Fe^{2+} , as determined by the 1, 10-phenanthroline (Phen) indicator where the coordination of Phen and Fe^{2+} turns the brown INFeD solution to light-red.^[16] It accompanies by a newly emerged adsorption peak (~508 nm) in ultraviolet-visible (UV-vis) spectra^[17]

This article is protected by copyright. All rights reserved.

(Figure 1a; Figure S3, Supporting Information) and a pair of Fe XPS peaks at ~ 709.6 (Fe $2p^{3/2}$) and 722.6 eV (Fe $2p^{1/2}$) (Figure 1b), reconfirming the generation of Fe^{2+} in VC@INFeD.^[18] In addition, a stepwise deprotonation process was also revealed in this reaction, as proved by the pH increase from ~ 3.56 ($t = 0$) to 5.34 ($t = 6$ h) in aqueous (Table S1, Supporting Information). Based on these phenomena, we speculated the detailed reaction process, as shown in Figure 1d. After two steps of proton transfer, VC can reduce Fe^{3+} of INFeD to Fe^{2+} and forms a covalent linkage with it. Interestingly, apart from Fe^{2+} , we also find the presence of Fe^{3+} which is determined by the peaks at ~ 711.4 (Fe $2p^{3/2}$) and 724.4 eV (Fe $2p^{1/2}$).^[19] This means the coexistence of mixed-valence Fe states in VC@INFeD and their proportion exhibits feed-ratio dependence (Figure S4 and Table S2, Supporting Information).



This article is protected by copyright. All rights reserved.

Figure 1. Composition and structure of VC@INFeD. a) UV-vis absorptions and optical photographs (inset) of INFeD, VC@INFeD, and $(\text{NH}_4)_2\text{Fe}(\text{SO}_4)_2$ aqueous solution before and after treating by phen indicator. b) Fe 2p XPS spectra of the obtained VC@INFeD. c) FT-IR spectra of VC@INFeD, INFeD, VC, and DHA. d) The illustration of proposed reaction mechanisms of VC and INFeD for the formation of VC@INFeD. The FT-IR spectra of DME (e) and DOL (f) solvents with or without the presence of VC@INFeD.

Using Fourier-transform infrared (FT-IR) and XPS spectroscopies, we verified the proposed reaction path. Figure 1c shows the FT-IR spectra of VC, INFeD, and VC@INFeD in a range of 1200 to 2400 cm^{-1} . Notably, the enol form of VC exhibits strong peaks at ~ 1651 ($-\text{C}=\text{C}-$) and 1749 cm^{-1} ($-\text{C}=\text{O}$). After reacting with INFeD, these peaks disappear and a ketone form ($\text{R}-(\text{C}=\text{O})-(\text{C}=\text{O})-\text{R}$) at ~ 1764 cm^{-1} is generated and detected, consistent with the fingerprint peak of dehydrogenated VC (DHA, indigo-blue line). In contrast to that of the pure DHA (~ 1772 cm^{-1}), the $\text{R}-(\text{C}=\text{O})-(\text{C}=\text{O})-\text{R}$ peak of VC@INFeD shifts to ~ 1764 cm^{-1} ; whereas the Fe 2p XPS peak of VC@INFeD moves significantly to a lower binding energy (Figure 1b; Figure S5, Supporting Information), as compared to INFeD. This demonstrates that the coordination occurs between the electron-donating $\text{R}-(\text{C}=\text{O})-(\text{C}=\text{O})-\text{R}$ groups of oxidized VC (DHA) and the electron-withdrawing Fe^{2+} groups of reduced INFeD,^[20] as shown in Figure 1d. Besides, the optimized DFT model of VC@INFeD confirms this configuration (Figure 1d; Figure S6, Supporting Information).

Moreover, we found that the VC@INFeD can obviously affect solvation clusters of Li^+ /LiPSs in the

traditional ether-based electrolyte by changing their binding configurations. As shown in Figure 1e,f, after adding VC@INFeD into DME and DOL solvents, the characteristic peak of –OH in VC@INFeD (3251 cm^{-1}) shifts to higher wavenumbers (3348 cm^{-1} in DME; 3517 cm^{-1} in DOL), which could be ascribed to the formation of intermolecular hydrogen bonds (H–bonds) between VC@INFeD and DME or DOL solvent. Similar binding patterns were previously reported to regulate the solvation sheath of Li-ions for stable Li anode.^[21]

2.2. Interplays between VC@INFeD and LiPSs: The interplays between VC@INFeD and LiPSs were firstly visualized by the static adsorption and dynamic H-type electrolytic cell tests.^[22] As shown in Figure S7 (Supporting Information), the yellow Li_2S_6 solution would fade after treating by the VC, DHA, INFeD, and VC@INFeD, respectively, for 12 h with a color depth order of $\text{Li}_2\text{S}_6 > \text{VC} > \text{DHA} \approx \text{INFeD} > \text{VC@INFeD}$, demonstrating highest LiPS absorptivity of the VC@INFeD. Thanks to the formation of H–bonds between VC@INFeD and solvated LiPSs, the VC@INFeD can capture nearly all Li_2S_6 in 20 seconds (Figure S8 and Video S1, Supporting Information), in sharp contrast to the traditionally slow LiPS adsorption process (for hours at least) that is the bottleneck of subsequent sulfur conversions. Moreover, for acquiring its LiPS elimination capability under battery operating conditions, we used various sulfur cathodes (CNTs/VC@INFeD, CNTs/INFeD, CNTs/VC, and CNTs) coupled with a Li metal sheet counterpart in Li_2S_6 catholyte (2 mM, 4 mL) to assemble H-type electrolytic cells which took photos after 0, 5, 10 cycles. Beginning with the same typical Li_2S_6 color, the Li_2S_6 catholyte of H-type cells gradually faded (Figure S9, Supporting Information) in all cells and swiftly bleached out in CNTs/VC@INFeD at a CV sweeping rate of 1.0 mV s^{-1} , which indicates the best LiPS adsorption/conversion ability of the VC@INFeD.

This article is protected by copyright. All rights reserved.

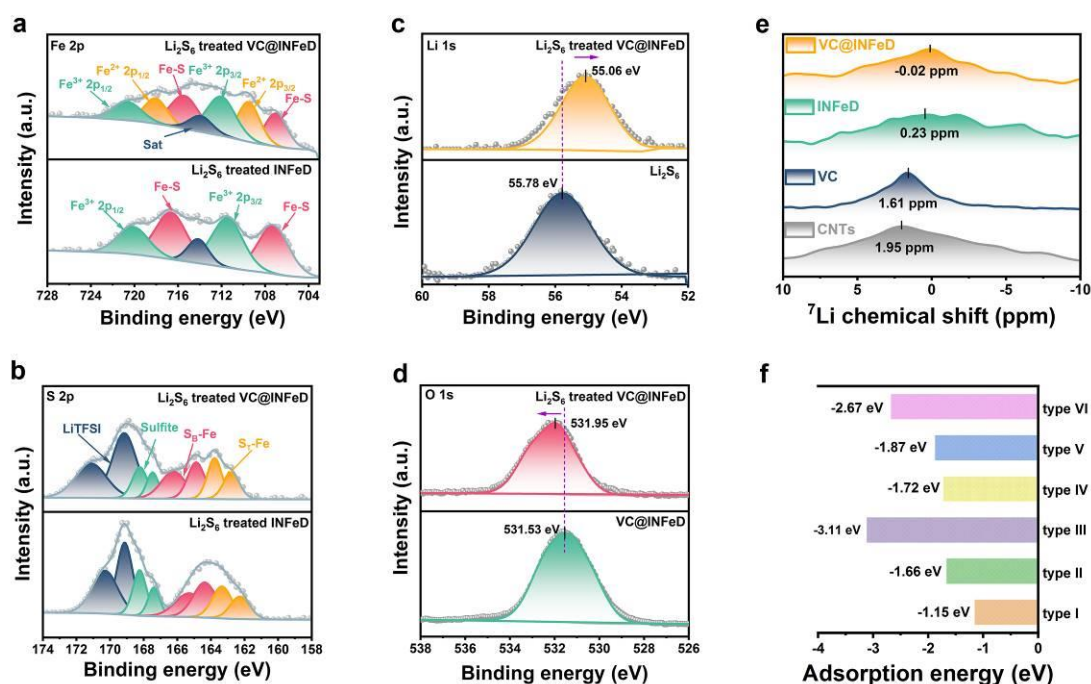


Figure 2. Mechanism studies of the interactions between VC@INFeD and LiPSs. a) Fe 2p and b) S 2p XPS spectra of Li₂S₆ treated VC@INFeD and INFeD, respectively. c) Li 1s and d) O 1s XPS spectra of Li₂S₆, VC@INFeD, and Li₂S₆ treated VC@INFeD. e) ⁷Li solid-state NMR spectra of CNTs, VC, INFeD, and VC@INFeD after treating by 20 mM Li₂S₆ solution for 24 h. f) DFT simulated Li₂S₆ adsorption energies on various O-containing sites of VC@INFeD.

To further elucidate the adsorption mechanism, in addition to the H–bond assisted LiPS solvation structure transfer, we checked the chemical/electronic evolutions of the INFeD and VC@INFeD cathodes in the desolvation process by XPS measurements and solid-state ⁷Li nuclear magnetic resonance (⁷Li NMR) spectroscopies after dipping them in Li₂S₆ catholyte for 24 h and then evaporating in an Ar-filled glovebox for dryness. As shown in **Figure 2a**, we found two distinct Fe 2p

This article is protected by copyright. All rights reserved.

XPS peaks both in Li_2S_6 treated INFeD ($\sim 716.72/707.34$ eV) and Li_2S_6 treated VC@INFeD ($\sim 716.54/707.03$ eV) which could be assigned to Fe–S bonds, resulting from Fe atoms of INFeD and S atoms of LiPSs .^[23] This point was confirmed by the S 2p XPS spectra and corresponding deconvolution analysis (Figure 2b). Influenced by Fe^{2+} generation, as compared to Li_2S_6 treated INFeD (165.33/164.31 and 163.34/162.23 eV), the bridge S (S_B) and terminal S (S_T) of Li_2S_6 treated VC@INFeD were shifted to higher fields (166.22/164.93 and 163.82/162.81 eV), contrary to the shifts of above mentioned Fe 2p peaks (Figure 2a), confirming the Fe–S bond formation.^[24] Besides, when compared to S 2p data of Li_2S_6 treated CNTs (164.24/163.52 and 162.64/161.71 eV, Figure S10, Supporting Information), the higher binding energy shifts of S_B and S_T in Li_2S_6 treated INFeD and VC@INFeD lead to decreased electron density, suggesting its mediating effects on sulfur conversions. Apart from S 2p variations, we also saw a lower binding energy shift of Li 1s XPS peak by 0.7 eV in Li_2S_6 -treated VC@INFeD compared with that of the pure Li_2S_6 (55.78 eV) (Figure 2c). Accordingly, the O 1s peak was shifted toward higher binding energy after Li_2S_6 treating (Figure 2d). This indicates a strong electron transfer exists from O atoms of VC@INFeD to Li atoms of Li_2S_6 which results in $\text{Li}\cdots\text{O}$ bond formation, namely Li–bond, according to previous reports.^[25]

A ^7Li NMR study was further performed to identify Li–bond since its chemical shift is quite sensitive to the surrounding environment (Figure 2e).^[26] In the case of Li_2S_6 -treated CNTs, a broad ^7Li resonance peak appears at ~ 1.95 ppm; while it downshifts to ~ 1.61 , 0.23, and -0.02 ppm of Li_2S_6 -treated VC, Li_2S_6 -treated INFeD, and Li_2S_6 -treated VC@INFeD, respectively. This suggests that the Li nucleus is more shielded by different types of O species in INFeD and VC due to the formation of multiple Li–bonds and it shows the strongest shielding effect in VC@INFeD. Typically, the binding

This article is protected by copyright. All rights reserved.

energy of Li–bond is much smaller than that of typical Li–O chemical bond (341 kJ mol^{-1}) because Li is more shared between S and O atoms in the former connection.^[27] Therefore, the Li^+ transfer barrier on VC@INFeD can be reduced and that may contribute to a fast Li^+ migration/supplement. To simulate this process, six typical theoretical models were constructed for calculating the binding energy of various O-containing groups in VC@INFeD toward Li_2S_6 species (Figure 2f; Figure S11, Supporting Information). It shows small binding energy of Li–bond (Type I, -1.15 eV) for the configuration of Li_2S_6 on dextran chains of INFeD that is far away from connection sites with VC. As the binding site approaches the connection site, the Li–bond energy increases simultaneously (Type II, -1.66 eV) and reaches a peak at the connection site (Type III, -3.11 eV), which may be affected by dual anchoring sites (Fe–S and Li–bonds) of VC@INFeD. A similar tendency can also be seen in the ferric hydroxide part of INFeD (Type IV, -1.72 eV) and VC (Type V, -1.87 eV ; Type VI, -2.67 eV). It should be noted that this binding energy gradient can impel LiPSs flow along with dextran chains of INFeD to VC@INFeD connection sites via Li–bonds, and thus helps to enrich LiPSs on catalysts. After that, multivalent Fe ($\text{Fe}^{3+}/\text{Fe}^{2+}$) sites bonded with LiPSs (through Fe–S bonds) at connection sites and further assisted their conversions. As a result, the interplays, mainly through H/Li–bonds and Fe–S bonds, lead to the LiPS enrichment in VC@INFeD and extract them out from the electrolyte, exhibiting ultra-fast and completely LiPS elimination.

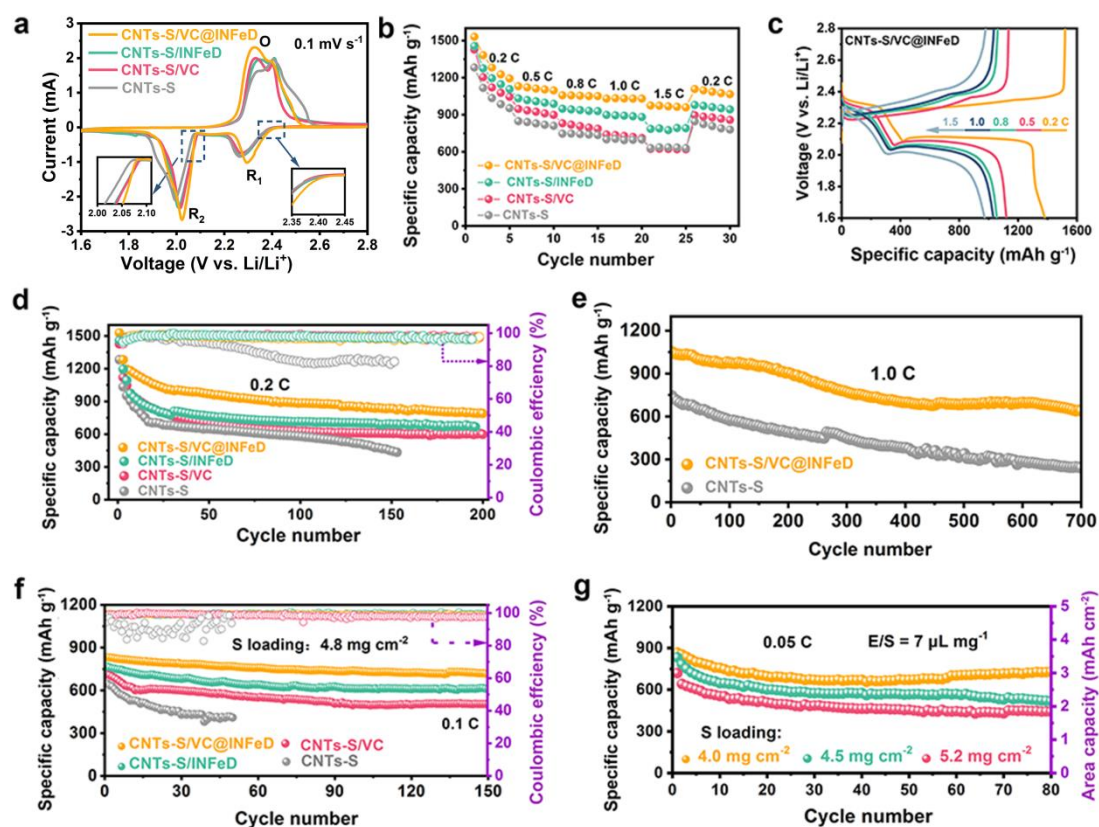


Figure 3. Electrochemical performances of Li-S batteries with VC@INFeD. a) CV profiles of CNTs-S, CNTs-S/VC, CNTs-S/INFeD, and CNTs-S/VC@INFeD cathodes at a scanning rate of 0.1 mV s^{-1} and a voltage range of 1.6–2.8 V. Insets are the magnification of corresponding reduction curves at 2.30–2.45 V and 2.00–2.10 V. b) Rate (0.2, 0.5, 0.8, 1.0, and 1.5 C) of the CNTs-S, CNTs-S/VC, CNTs-S/INFeD, and CNTs-S/VC@INFeD cells and c) voltage-capacity profiles of CNTs-S/VC@INFeD under 0.2 C, 0.5 C, 0.8 C, 1.0 C, and 1.5 C. d) cycling performances at 0.2 C of the CNTs-S, CNTs-S/VC, CNTs-S/INFeD, and CNTs-S/VC@INFeD cells. e) Long-term cycling performances of the CNTs-S and CNTs-S/VC@INFeD cathodes at 1.0 C. f) Cycling stability of CNTs-S, CNTs-S/VC, CNTs-S/INFeD, and CNTs-S/VC@INFeD cathodes at 0.1 C with a high sulfur loading of $\sim 4.84 \text{ mg cm}^{-2}$. g) Galvanostatic cycling performances of the CNTs-S/VC@INFeD cathode at 0.05 C with an E/S ratio of $7 \text{ }\mu\text{L mg}^{-1}$ and a sulfur loading of 4.0,

This article is protected by copyright. All rights reserved.

4.5, 5.2 mg cm⁻², respectively.

2.3. Electrochemical Performances: The rapid enrichments and complete conversions of LiPSs on VC@INFeD can be directly reflected in its electrochemical performances, which were characterized by the assembled Li-S coin cells and evaluated by cyclic voltammetry (CV) and galvanostatic charge/discharge techniques. To highlight the merits of VC@INFeD, the CNTs-S, CNTs-S/VC, and CNTs-S/INFeD cathodes were also assembled and measured. As shown in Figure S12 (Supporting Information), CV profiles of these four cathodes under a sweeping rate of 0.1 mV s⁻¹ were respectively overlapped and stabilized after an initial activation cycle; the current-voltage functions were plotted (Figure 3a) where an anodic and two cathodic peaks were found, which correspond to S₈ to soluble LiPSs (Peak R₁), soluble LiPSs to Li₂S₂/Li₂S (Peak R₂), and Li₂S₂/Li₂S back to soluble LiPSs or S₈ (Peak O), respectively.^[26] In contrast to the other three cathodes, the CNTs-S/VC@INFeD shows the smallest voltage gap between the reduction (Peak R₁, ~2.30 V; Peak R₂, ~2.03 V) and oxidation (Peak O, ~2.33 V) peaks and yet the highest current densities (Figure S13, Supporting Information). According to the Faraday's law, this means the VC@INFeD could substantially reduce battery polarization and improve reaction kinetics, as demonstrated by the smallest voltage hysteresis and highest conductance (dl/dU) of CV differential deformations (Figure S14, Supporting Information).^[14] Of note, the observed earlier CV current dropping at Peak R₁ (inset, right) for the INFeD-containing electrodes (CNTs-S/VC@INFeD and CNTs-S/INFeD) and at Peak R₂ (inset, left) for the VC-containing electrodes (CNTs-S/VC@INFeD and CNTs-S/VC) suggest that INFeD promotes the reduction of long-chain LiPSs; while VC promotes the reduction of short-chain LiPSs.

As a result, the CNTs-S/VC@INFeD cathode exhibits a much-enhanced rate and cycling performance.

This article is protected by copyright. All rights reserved.

It delivered a higher discharge capacity of 1530, 1130, 1057, 1030, and 974 mAh g⁻¹ at 0.2, 0.8, 0.8, 1.0, and 1.5 C, respectively, with longer and flatter discharge plateaus as well lower voltage hysteresis than that of the control cells (CNTs-S (1281, 847, 746, 700, and 629 mAh g⁻¹), CNTs-S/VC (1427, 946, 830, 739, and 624 mAh g⁻¹), and CNTs-S/INFeD (1455, 1031, 947, 898, and 785 mAh g⁻¹) (Figure 3b,c; Figure S15, Supporting Information). As the current rate turns swiftly back to 0.2 C, a highly reversible discharge capacity was achieved (1107 mAh g⁻¹). The decreased overpotential, superior rate capability, and high reversibility of the CNTs-S/VC@INFeD cathode resulted from much improved electrochemical kinetics, which was further revealed by electrochemical impedance spectroscopies (EIS). When ceasing the cell at 1.6 V, the EIS profiles and corresponding equivalent fitting circuit models were recorded where the semicircle in the high-frequency region reflects the charge-transfer resistance (R_{ct}); the semicircle in the medium-frequency region indicates the mass transportation resistance (R_{mt}) of LiPSs. Of all, as expected, the CNTs-S/VC@INFeD cathode exhibited much smaller R_{ct} (20.8~28.9 Ω) and R_{mt} (13.1~15.3 Ω) after various cycles (Figure S16–17 and Table S3–6, Supporting Information).^[27]

Figure 3d shows the cycling performance and Coulombic efficiency of the cell with CNTs-S/VC@INFeD cathode at 0.2 C. The initial discharge capacity is 1528 mAh g⁻¹ and it maintains 788 mAh g⁻¹ after 200 cycles with a mean capacity decay rate of ~0.23% per cycle and high Coulombic efficiency of 98.4%. By contrast, the control cells (CNTs-S/INFeD and CNTs-S/VC) have a lower initial discharge capacity of 1455 and 1427 mAh g⁻¹, and the capacity quickly drops to 776 and 763 mAh g⁻¹ after 30 cycles, and 666 and 597 mAh g⁻¹ after 200 cycles, respectively. Nevertheless, it is still better than the pristine CNTs-S cell with an initial discharge capacity of 1281 mAh g⁻¹ and expired after 153

This article is protected by copyright. All rights reserved.

cycles. While the CNTs-S/VC@INFeD cell can still survive even under a high rate of 1.0 C after 700 continuously cycles and retains a high capacity of 642 mAh g⁻¹ (Figure 3e; Figure S18, Supporting Information). Besides, the cycling performance of thick cathodes (Figure 3f) was also evaluated at 0.1 C with a high sulfur loading of ~4.8 mg cm⁻² (calculated by the S mass). As expected, the CNTs-S/VC@INFeD cell shows much higher initial discharge capacity (832 mAh g⁻¹) and capacity retention (717 mAh g⁻¹ after 150 cycles) than control cells (CNTs-S/INFeD, 766 and 611 mAh g⁻¹; CNTs-S/VC, 710 and 503 mAh g⁻¹; CNTs-S, 646 mAh g⁻¹ and expired after 50 cycles). Under lean electrolyte conditions (electrolyte/sulfur ratio (E/S) of ~7 μL mg⁻¹), as shown in Figure 3g, the CNTs-S/VC@INFeD cells with sulfur loading of 4.0, 4.5, and 5.2 mg cm⁻² afford a discharge capacity of 727, 516, and 441 mAh g⁻¹, respectively, after 80 cycles.^[28] The coin cell study proves that VC@INFeD can be successfully applied as a sulfur mediator in Li-S batteries to rationally improve their cycling capacity and stability.^[29]

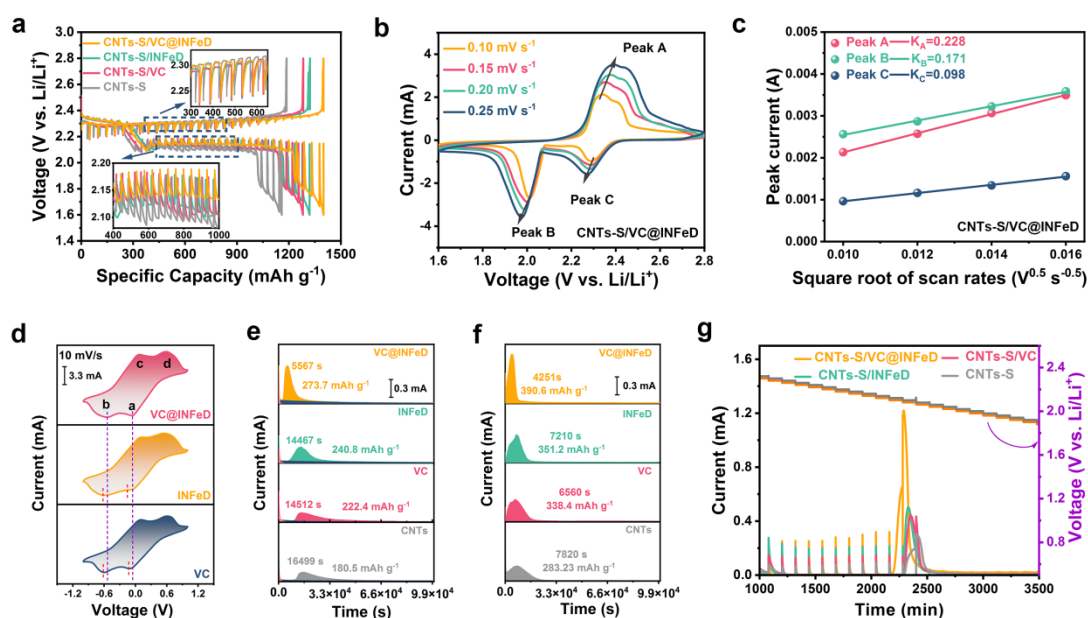


Figure 4. Characterization of sulfur conversion kinetics. a) Galvanostatic intermittent titration

This article is protected by copyright. All rights reserved.

technique (GITT) tests of the CNTs-S/VC@INFeD, CNTs-S/INFeD, CNTs-S/VC, and CNTs-S cells. b) CV profiles of the CNTs-S/VC@INFeD cell at scanning rates from 0.10 to 0.25 mV s⁻¹. c) Scanning rate-dependent parameters of the CNTs-S/VC@INFeD cell for calculation of Li⁺ diffusion coefficient by CV redox peaks at A, B, and C. d) CV profiles of the VC, INFeD, and VC@INFeD electrodes in Li₂S₆ symmetric cells. Potentiostatic discharge and charge profiles of Li₂S e) nucleation and f) decomposition on the CNTs, VC, INFeD, and VC@INFeD electrodes. g) Potentiostatic intermittent titration technique (PITT) measurements of CNTs-S/VC@INFeD, CNTs-S/INFeD, CNTs-S/VC, and CNTs-S cells.

2.4. Structure-Activity Relationship: In order to reveal the underlying reasons for battery performance improvements, we firstly studied the reaction kinetics of the assembled Li–S coin cells which was evaluated by Li⁺ chemical diffusion coefficient (D_{Li^+}) and characterized by both galvanostatic intermittent titration (GITT) and scanning rate-dependent CV techniques. Generally, GITT is a real-time tool that provides time-dependent voltage information and kinetic evolutions of both the equilibrium voltage and the relaxation behavior during battery discharging and charging.^[30] As illustrated in **Figure 4a**, we compared GITT curves of CNTs-S/VC@INFeD and control cells (CNTs-S, CNTs-S/VC, and CNTs-S/INFeD) during the first discharge/charge step where the voltages at the end of each galvanostatic step as well as relaxation step were plotted as a function of specific discharge/charge capacity. For the CNTs-S/VC@INFeD cell, the second discharge plateau exhibits a much smaller potential gap (~55 mV) between the reduction voltage and relaxation open-circuit voltage than other cells (CNTs-S, 120 mV; CNTs-S/INFeD, 77 mV; CNTs-S/VC, 85 mV), accompanied by greatly reduced IR-drop, after equilibration for 2 h; the charge profiles show the same pattern of

This article is protected by copyright. All rights reserved.

changes. It confirms that the VC@INFeD additive can relieve the cell polarization and promote the Li^+ transfer kinetics. To quantitatively determine Li^+ transfer kinetics, the scanning rate-dependent CV tests for all cells were performed. Based on the Randles–Sevcik equation:^[31]

$$I_p = 2.69 \times 10^5 \cdot n^{1.5} \cdot S \cdot D_{\text{Li}^+}^{0.5} \cdot v^{0.5} \cdot C_{\text{Li}^+}$$

where I_p indicates the peak current density, n represents the number of electrons transferred in the reaction, S is the electrode area, D_{Li^+} provides the diffusion coefficient of Li^+ , v is the scanning rate, and C_{Li^+} is the Li^+ concentration in the electrolyte. We fitted D_{Li^+} and $v^{0.5}$ at each redox peak (A, B, and C) of these four cells (Figure 4b,c; Figure S19, Supporting Information) and a linear functional relationship was obtained which implies typical ion diffusion-controlled reactions. As for the CNTs-S/VC@INFeD cell, D_{Li^+} at cathodic peak A and B is 7.0×10^{-8} and $4.0 \times 10^{-8} \text{ cm}^2 \text{ s}^{-1}$, and at anodic peak C is $1.3 \times 10^{-8} \text{ cm}^2 \text{ s}^{-1}$, respectively, for which the values are up to ~ 2.0 times larger than those of the CNTs-S/INFeD (5.6×10^{-8} , 2.1×10^{-8} , and $6.6 \times 10^{-9} \text{ cm}^2 \text{ s}^{-1}$) or CNTs-S/VC cell (4.4×10^{-8} , 2.9×10^{-8} , and $5.0 \times 10^{-9} \text{ cm}^2 \text{ s}^{-1}$), in contrast to lowest values of pristine CNTs-S cell (3.2×10^{-8} , 1.6×10^{-8} , and $2.1 \times 10^{-9} \text{ cm}^2 \text{ s}^{-1}$). The highest D_{Li^+} values signify good Li^+ transport/supplement capability and rapid reaction kinetics of the CNTs-S/VC@INFeD cell, probably due to the formation of multiple $\text{Li}\cdots\text{O}$ bonds as mentioned above.^[32]

According to previous reports, the dynamic changes of Li^+ will be accompanied by the changes of sulfur counterparts. Hence, we further investigated the sulfur evolutions by means of Li_2S_6 symmetrical cells, Li_2S nucleation/decomposition, and potentiostatic intermittent titration technique (PITT) tests as well as ex/in-situ spectroscopies. First of all, to study liquid–liquid sulfur

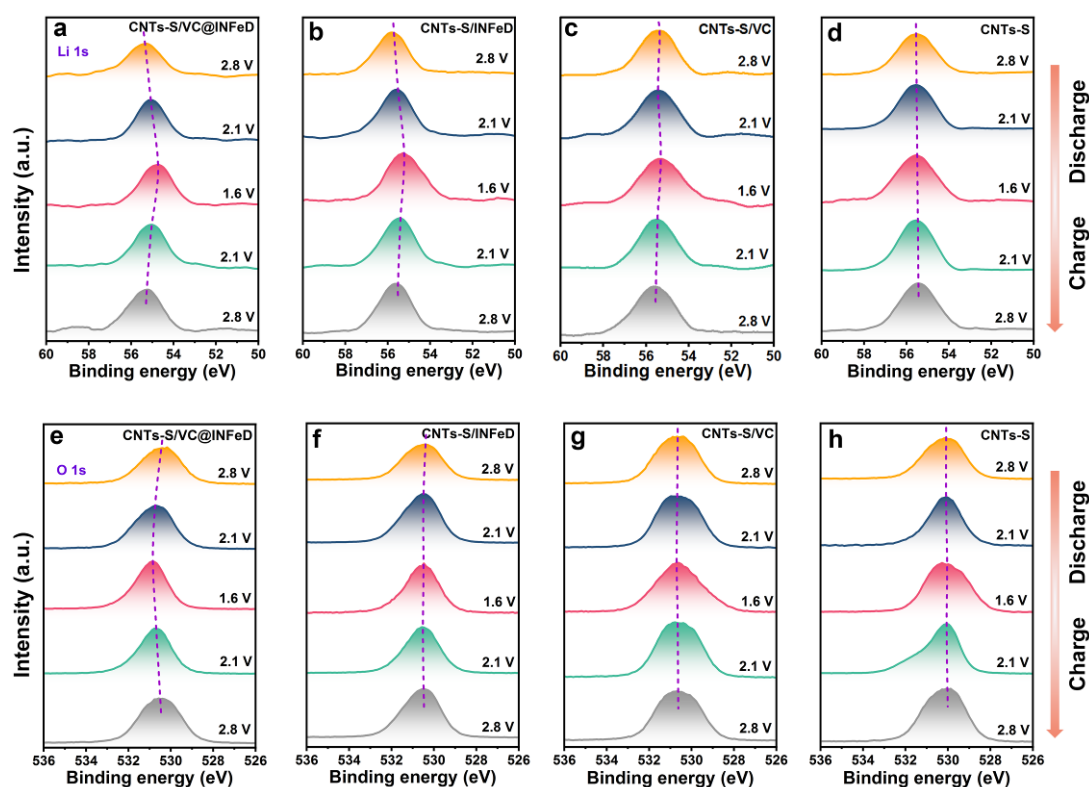
This article is protected by copyright. All rights reserved.

transformations (reactions between long-chain LiPSs and short-chain LiPSs), symmetrical cells were assembled with two identical VC, INFeD, or VC@INFeD electrodes and Li_2S_6 electrolyte (0.25 M, 20 μL). At a CV scanning rate of 10 mV s^{-1} , the VC@INFeD electrode shows two pairs of redox peaks at $-0.06/0.06$ and $-0.55/0.55 \text{ V}$ (**Figure 4d**) which represent the redox reactions of long-chain and short-chain LiPS conversions,^[23] respectively; whereas these peaks in both INFeD ($-0.10/0.10$ and $-0.60/0.60 \text{ V}$) and VC ($-0.12/0.12$ and $-0.62/0.62 \text{ V}$) symmetrical cells shift to higher voltages and the CV integral area is significantly reduced from 7.06 (VC@INFeD) to 6.35 (INFeD) and 5.41 mW (VC) (Figure S20, Supporting Information), which indicate that the liquid–liquid conversions can be effectively enhanced by the VC@INFeD. Subsequently, the reduction of short-chain LiPSs on various cells to form Li_2S (liquid–solid conversions) was monitored by the potentiostatic Li_2S nucleation tests at 2.04 V (see experimental details in Supporting Information). Through fitting $i-t$ curves (Figure 4e), we ranked the capacity that corresponds to Li_2S deposition as VC@INFeD (273.7 mAh g^{-1}) > INFeD (240.8 mAh g^{-1}) > VC (222.4 mAh g^{-1}) > CNTs (180.5 mAh g^{-1}) with a response time of 5567, 14186, 14467, and 16499 s, respectively.^[33] By contrast, the VC@INFeD cell shows much faster responsivity, higher current density, and larger Li_2S precipitation capacity, which demonstrates more LiPSs are rapidly transformed to Li_2S by assisting of VC@INFeD mediator. During charge, the Li_2S decomposition behavior (solid–liquid conversions), from Li_2S to LiPSs, was investigated via potentiostatically charging the cells at 2.4 V. As shown in Figure 4f, the VC@INFeD displays a higher Li_2S decomposition capacity and an earlier oxidation peak (390.6 mAh g^{-1} , 4251 s) than that of the INFeD (338.4 mAh g^{-1} , 7210 s), VC (351.2 mAh g^{-1} , 6560 s), and CNTs (283.2 mAh g^{-1} , 7820 s) cells, demonstrating excellent decomposition ability of Li_2S .^[34] Both Li_2S nucleation and decomposition tests prove that VC@INFeD can accelerate bidirectional conversion reactions between short-chain

This article is protected by copyright. All rights reserved.

LiPSs and Li_2S .

For evaluating the whole process at a battery level, we used the PITT test to semi-quantitatively determine the number of sulfur conversions whose curves at higher titration potential (> 2.10 V) correspond to the reduction of long-chain LiPSs to short-chain LiPSs; the lower titration potential (< 2.10 V) corresponds to a liquid-solid transformation of short-chain LiPSs to solid $\text{Li}_2\text{S}_2/\text{Li}_2\text{S}$ sediments.^[35] The CNTs-S/VC@INFeD cell, as shown in Figure 4g, has a faster and higher peak current (1.103 mA, 2286 min) compared to that of the CNTs-S/VC (0.802 mA; 2353 min), CNTs-S/INFeD (0.826 mA; 2330 min), and CNTs-S (0.774 mA; 2412 min) cells, which means VC@INFeD can effectively catalyze the sulfur species and greatly improve sulfur utilization.



This article is protected by copyright. All rights reserved.

Figure 5. Li–bond chemistry in sulfur catalysis. Semi-in situ Li 1s and O 1s XPS spectra of the cell with (a, e) CNTs-S/VC@INFeD, (b, f) CNTs-S/INFeD, (c, g) CNTs-S/VC, and (d, h) CNTs-S cathode at different charge and discharge depths: fully charged state at 2.8 V, half-discharged state at 2.1 V, fully discharged state at 1.6 V, half-charged state at 2.1 V, and fully re-charged state at 2.8 V.

2.5. Li–bond Chemistry and Catalytic Mechanisms: To clarify the underlying mechanisms, a series of semi-in situ Li 1s and O 1s XPS data was collected from the batteries discharged/charged to different depths (fully charged to 2.8V, half-discharged to 2.1 V, fully discharged to 1.6 V, half-charged to 2.1 V, and fully re-charged to 2.8 V). As shown in **Figure 5a**, with the discharge depth increase, the Li 1s peaks in the CNTs-S/VC@INFeD gradually shift to lower binding energy (55.27 eV at 2.8, 55.05 eV at 2.1, 54.82 eV at 1.6 V), which is attributed to the electron transfer from the O atom of VC@INFeD to the Li atom of LiPSs that results in the formation of Li···O bond, as proved by the higher binding energy shift of O 1s peaks (530.49 eV at 2.8, 530.71 eV at 2.1, 530.89 eV at 1.6 V) (Figure 5e). Upon charging, the shifts of Li 1s and O 1s peaks are reversed, which is indicative of reversible electron transfer from LiPSs to VC@INFeD. As comparative experiments, the semi-in situ Li 1s and O 1s XPS measurements were conducted on the CNTs-S/INFeD (Figure 5b,f), CNTs-S/VC (Figure 5c,g), and CNTs-S cathodes (Figure 5d,h). It shows that almost no Li 1s signal deviation occurs in CNTs-S/VC (55.45 eV) and CNTs-S (55.44 eV) cathodes during discharge and charge, indicating that there is no efficient Li···O bond coordination in the system. Accordingly, the Li 1s peak for the CNTs-S/INFeD cathode shifts to the lower binding energy with discharge and recovers to higher binding energy in charge, reflecting the crucial role of INFeD in the Li···O bond formation. Based on the Li–bond formation theory (the atom with high electronegativity captures electron from the Li atom, making Li

This article is protected by copyright. All rights reserved.

atom a good electron acceptor, and it accepts electron from outer strong electronegative elements after that, causing intense chemical interaction), we speculate that the formation of Li...O bond mainly caused by the Li...O-H bridge through LiPSs and -OH of INFeD. A large number of Li...O bond formation implies the Li-supplementation is substantially enhanced by INFeD, which can not only facilitate the transfer of LiPSs on the catalyst surface, but also motivate subsequent conversions.

In-situ spectroscopies are powerful methods to catch intermediate signals of Li-S batteries which are crucial for elucidating LiPS transformation pathways. As shown in Figure S21 (Supporting Information), from in-situ Raman spectra we found that the VC@INFeD catalyst can mediate the initial S_8 transformation (S_8 to LiPSs) and endow the battery with high sulfur utilization. Furthermore, in-situ ultraviolet-visible (UV-vis) spectroscopies were carried out on various cells (CNTs, CNTs/VC, CNTs/INFeD, and CNTs/VC@INFeD), after considering LiPS intermediates have different absorption bands, which were discharged in Li_2S_8 and Li_2S_4 catholyte and charged in Li_2S_3 catholyte, respectively. Notably, the oxidized VC (DHA) which coordinates with partially reduced INFeD in the formation of VC@INFeD was also considered as a control group. As shown in Figure S22 (Supporting Information), all the cells show characteristic absorption peaks at ~492, 475, 420, and 617 nm that can be assigned to S_8^{2-} , S_6^{2-} , S_4^{2-} , and S_3^{*-} anions, respectively.^[14] The corresponding absorbance intensities were collected and normalized and plotted as a function of voltage. In Li_2S_8 catholyte, by contrast, the INFeD containing cells (CNTs/INFeD and CNTs/VC@INFeD) show much more rapidly decreased S_8^{2-} intensities and almost unchanged S_3^{*-} signals during discharge (**Figure 6a**); while in Li_2S_4 catholyte, the S_4^{2-} intensity of VC containing cells (CNTs/VC, CNTs/DHA, and CNTs/VC@INFeD) decrease more sharply (**Figure 6b**). These reconfirm that INFeD additives can accelerate long-chain LiPS

This article is protected by copyright. All rights reserved.

transformations and VC can induce short-chain LiPS conversions. Moreover, in charge process, as shown in Figure 6c, we monitored the S_6^{2-} and S_3^{*-} signals in Li_2S_3 catholyte. The VC@INFeD also exhibited a much faster S_6^{2-} intensity increase and S_3^{*-} intensity decrease, showing good catalytic effects on Li_2S decomposition. As a result, the VC@INFeD cell demonstrates good cascade catalytic properties on both long-chain and short-chain LiPSs.

To elucidate the catalytic mechanisms, semi-in situ S 2p and Fe 2p XPS spectra were also performed. As shown, the S 2p data present characteristic S_T (~162.1/161.2 eV) and S_B (~164.3/162.9 eV) signals which can be roughly assigned to LiPSs and Li_2S_2/Li_2S , respectively. With the depth of discharge increase, the S_B peak intensity of CNTs-S/VC@INFeD (Figure 6d) decreases and eventually disappears at 1.6 V, accompanied by a peak displacement from ~164.3/162.9 eV (2.8 V) to ~163.5/162.7 eV (2.1 V); while the S_T peak (162.1/161.2 eV) intensity increases throughout the whole discharge process with subtle peak position changes. This means a complete LiPS depletion occurs in the CNTs-S/VC@INFeD cell and it finally be catalyzed to Li_2S_2/Li_2S precipitants. In the charge process, as expected, both S_B and S_T peaks are recovered to their initial states, showing a good sulfur catalysis reversibility of the VC@INFeD.^[36] In stark contrast, as for the CNTs-S/INFeD (Figure 6e) and CNTs-S/VC cells (Figure S23a, Supporting Information), the initially strong S_T and S_B peaks at 2.8 V should be attributed to unreacted Li_2S and LiPSs in the previous cycle, respectively. During discharge, for both samples, the S_B peak intensity decreases and the S_T peak intensity increases simultaneously, but the trends in the charge process are very reverse, obviously different from the CNTs-S/VC@INFeD cell.^[21] Similar S 2p signal variations can also be found in the CNTs-S reference cell (Figure S23b, Supporting Information). Notably, the coexistence of S_B and S_T signals at 1.6 and 2.8 V implies incomplete

This article is protected by copyright. All rights reserved.

transformations of LiPSs in control cells and indicates that INFeD or VC alone is inefficient for LiPS conversions, inconsistent with the in-situ Raman results.

Moreover, the S 2p peak shifts were also considered as well as the Fe 2p data due to the Fe–S bond interactions. As shown in Figure 6f, in discharge, the Fe²⁺ proportion of the CNTs-S/VC@INFeD cell decreases, and the Fe³⁺ proportion increases gradually, which means Fe²⁺ undergoes an oxidation reaction that is complementary to the reduction of S. In addition, with the depth of discharge, both Fe²⁺ and Fe³⁺ peaks move to higher binding energy (Fe³⁺/Fe²⁺; 2.8 V: 729.4/712.0 eV and 725.9/706.4 eV; 2.1 V: 729.9/712.7 eV and 726.4/707.7 eV; 1.6 V: 732.1/713.0 eV and 727.7/708.7 eV, respectively) and S 2p peaks shift to lower binding energy (S_B; 2.8 V: 164.3/162.9 eV; 2.1 V: 163.5/162.7 eV; 1.6 V, disappear), indicating Fe in VC@INFeD is losing electron density to S atoms of LiPSs and that contributes to the break of S–S bonds from long-chain LiPSs to short-chain LiPSs. Similarly, a reverse peak shift tendency was seen in the charge process. However, as for the CNTs-S/INFeD cell (Figure 6g), it shows a smaller reversible peak shift (Fe³⁺; 2.8 V: 724.7/712.8 eV; 2.1 V: 725.2/713.2 eV; and 1.6 V: 725.3/713.4 eV) due to the lack of Fe²⁺ regulation. Nevertheless, the peak shift changes greatly at the potential range of 2.1 to 2.8 V regardless of charging or discharging, this corresponds to the fact that INFeD promotes long-chain LiPS conversions.

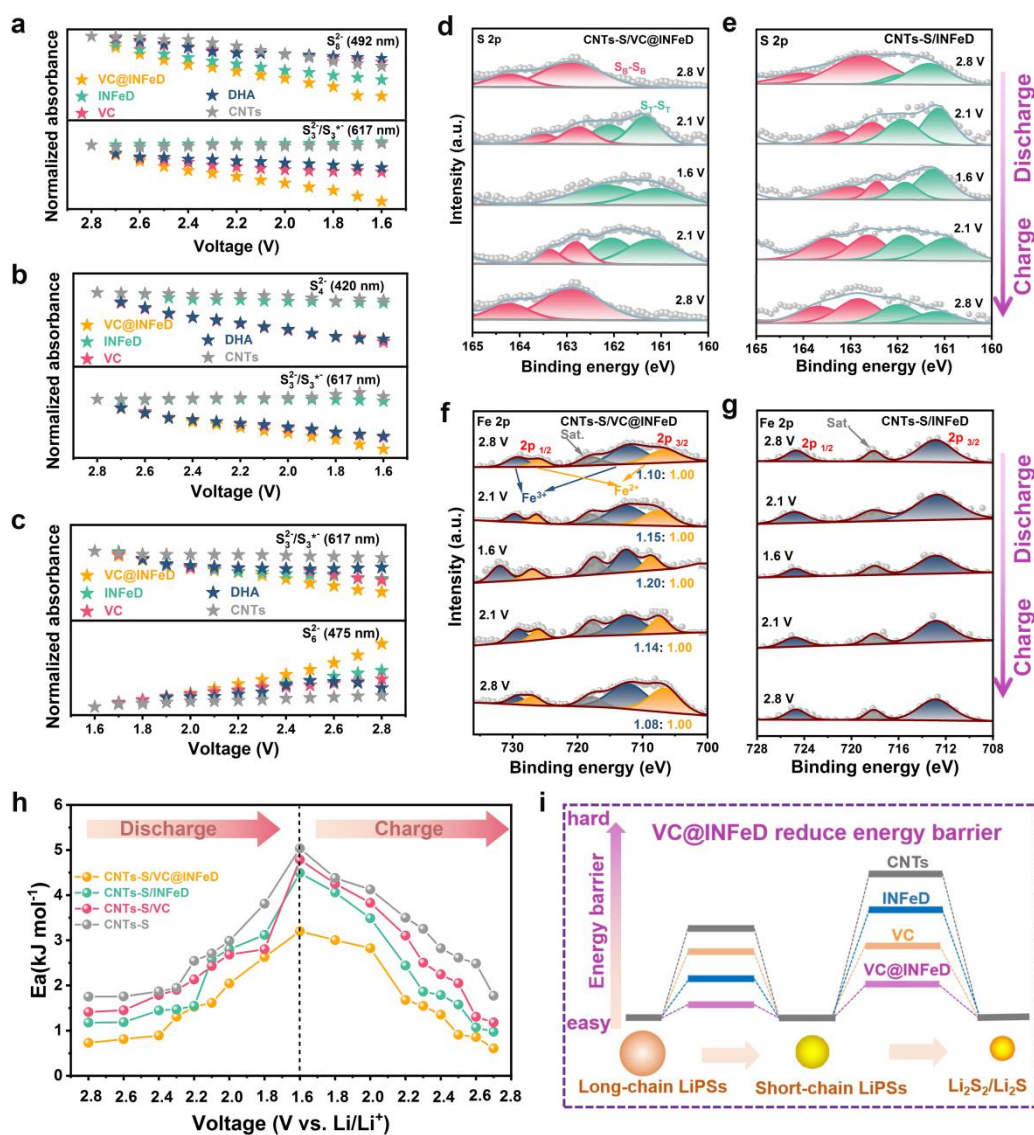


Figure 6. Dynamic sulfur conversion recorded by in/ex situ spectroscopies. Normalized absorbance of in-situ ultraviolet-visible (UV-vis) spectroscopies on the cell with CNTs /VC@INFeD, CNTs/INFeD, CNTs/DHA, CNTs/VC, and CNTs electrodes at different discharge/charge depths: a) S_8^{2-}/S_3^{*-} in Li_2S_8 catholyte and b) S_4^{2-}/S_3^{*-} in Li_2S_4 catholyte during discharge; and c) S_6^{2-}/S_3^{*-} in Li_2S_3 catholyte during charge. Semi-in situ S 2p and Fe 2p XPS spectra of the cell with (d, f) CNTs-S/VC@INFeD, (e, g) CNTs-S/INFeD under various discharge and charge depths. h) Voltage-dependent activation energy plots

This article is protected by copyright. All rights reserved.

collected from EIS spectra at various discharge/charge voltages and temperatures for the CNTs-S/VC@INFeD, CNTs-S/VC, CNTs-S/INFeD, and CNTs-S cells. i) Schematic illustration of stepwise sulfur catalytic conversions enabled by VC@INFeD.

Theoretically, the sulfur conversion difficulty of each step can be directly and fundamentally measured by the activation energy (E_a), which is experimentally collected and calculated by the electrochemical impedance spectra (EIS) at various voltages and temperatures (Figures 24–32, Supporting Information).^[37] Through fitting the Arrhenius equation, Figure 6h shows the E_a values of the CNTs-S, CNTs-S/VC, CNTs-S/INFeD, and CNTs-S/VC@INFeD cells as a function of charge/discharge voltage. In discharge, the E_a for all cells displays a relatively low value in the long-chain LiPS formation stage (2.8 to 2.2 V) and increases sharply for the formation of short-chain LiPSs and $\text{Li}_2\text{S}_2/\text{Li}_2\text{S}$ (2.2 to 1.6 V); while, in charge, the E_a value decreases slowly at the formation of short-chain LiPSs and $\text{Li}_2\text{S}_2/\text{Li}_2\text{S}$ (1.6 to 2.0 V) and then rapidly in forming long-chain LiPS and S_8 , which implies the rate-determining step in these cells is the formation/decomposition of $\text{Li}_2\text{S}_2/\text{Li}_2\text{S}$. By contrast, E_a of the CNTs-S/VC@INFeD cell shows a much lower value than that of the other cells over the entire discharge and charge cycle, exhibiting decreased reaction barriers and superior catalytic effects as well as facilitated both long-chain and short-chain LiPS conversions (Figure 6i). It is worth to note, the CNTs-S/VC and CNTs-S/INFeD cells present much lower E_a than that of the pristine CNTs-S, demonstrating positive effects of VC and INFeD additives on sulfur conversions. When compared to CNTs-S/VC, the CNTs-S/INFeD cell has much lower E_a for converting long-chain LiPSs at an expense of higher E_a for the formation of short-chain LiPSs in discharge, which indicates that INFeD is conducive to catalyze the reduction of long-chain LiPSs and VC has a better catalytic effect on the short-chain

This article is protected by copyright. All rights reserved.

LiPSs, in accordance with the in-situ UV-vis results. Obviously, a broadly reverse tendency in the charge process is observed in both cells where the CNTs-S/INFeD possesses comparatively lower E_a than the CNTs-S/VC, showing better catalytic effects of INFeD on the sulfur oxidation process.

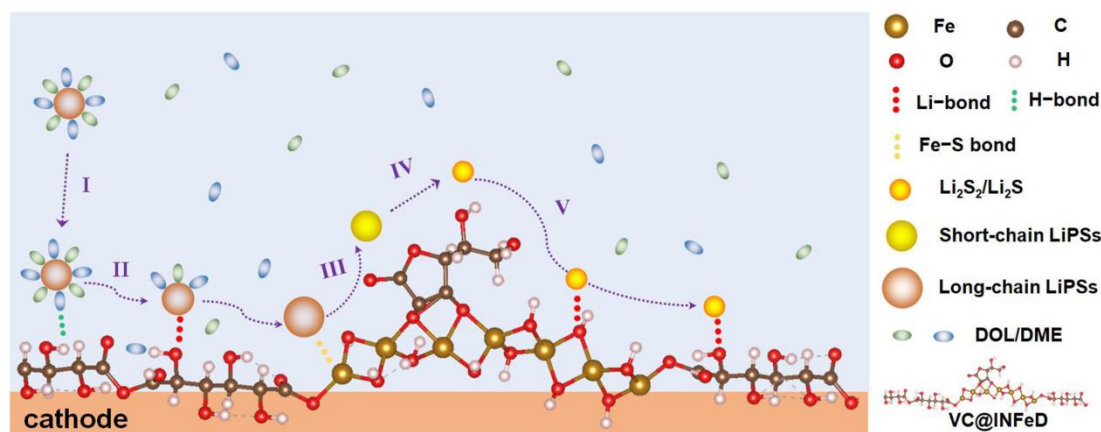


Figure 7. Schematic illustration of the VC@INFeD molecular catalyst on regulating Li-S chemistry: step I, the enrichment of solvated LiPSs at the VC@INFeD catalyst/electrolyte interface enabled by multiple H-bonds; step II, rapid desolvation and transfer of LiPSs on the VC@INFeD surface with the assistance of Li-bonds; step III, multivalent $\text{Fe}^{2+}/\text{Fe}^{3+}$ catalytic centers of INFeD promotes long-chain LiPS conversions; step IV, VC promotes the short-chain LiPS conversions; step V, Li-bond assists $\text{Li}_2\text{S}_2/\text{Li}_2\text{S}$ transfer.

Based on the above experimental results and theoretical simulations, we highlight the synergy of VC and INFeD for promoting the Li^+/LiPS transfer and further transformations. As illustrated in **Figure 7**, during the electrochemical process, the VC@INFeD molecular catalyst can bind with solvated Li^+ or LiPS clusters through the formation of H-bond, occurring between $-\text{OH}$ of INFeD and ether groups of

DOL/DME molecules (step I). With the depth of discharge increase, Li-bond is formed by substitution of H-bond on INFeD (step II) because the bond energy of Li-bond is much higher than H-bond. Notably, as compared to the chemical Li-O bond, the Li-bond has much weaker bond energy which is conducive to the transfer of anchored Li⁺/LiPSs on the catalyst. The process helps to accelerate Li⁺/LiPS de-solvation and anchor it on the catalyst, thus achieving localized high concentration Li⁺/LiPS distribution at the cathode/electrolyte interface. This satisfies the primary condition for catalytic reactions, that is, the enrichment of large amounts of substrates. Subsequently, as illustrated in Figure 6i, a cascade of LiPS transformations at different catalytic sites of VC@INFeD is achieved: Fe³⁺/Fe²⁺ of INFeD boost the cleavage of long-chain LiPSs (step III); while VC promotes the reduction of short-chain LiPSs (step IV). Unlike discharge, it is mainly the multivalent Fe states of INFeD that accelerate the oxidation reactions throughout the charge process. At last, by the virtue of Li-bonds, the final reduction products (Li₂S₂/Li₂S) are demonstrated to dissociate from the VC@INFeD catalyst and restore its catalytic activity (step V). As a result, the cell with CNTs-S/VC@INFeD cathode shows much improved electrochemical performance even under high sulfur loading and lean electrolyte.

3. Conclusion

In summary, we have successfully prepared a highly efficient VC@INFeD molecular catalyst for Li-S batteries, aiming to enrich high-concentration LiPS substrate distribution at the cathode/electrolyte interface and resolve subsequent sluggish sulfur transformations. The VC@INFeD catalyst can initially bind with solvated Li⁺/LiPSs from electrolyte through multiple H-bond and Li-bond, and then

This article is protected by copyright. All rights reserved.

transfer them to catalytic sites where INFeD boost the cleavage of long-chain LiPSs and the VC promotes the conversion of short-chain LiPSs. Consequently, the VC@INFeD can substantially reduce the energy barrier of each sulfur redox step and eliminate long-term presence of high LiPS concentrations in electrolyte, and as a result, inhibiting shuttle effects and endowing Li-S batteries with high sulfur utilization and superior cycling stability as well. We believed that this VC@INFeD molecular catalyst design in this work can not only provide insights on high performance Li-S batteries, but also open opportunities to innovate catalyst/electrolyte interface engineering in the fields such as liquid electrolyte and semi-solid flow energy storage devices.

Supporting Information

Supporting Information is available from the Wiley Online Library or from the author.

Acknowledgements

This research was funded in part by National Natural Science Foundation of China (Grant Nos. 51972238 and 22109119), Natural Science Foundation of Zhejiang Province (Grant No. LQ22B030003).

Conflicts of Interest

There are no conflicts to declare.

This article is protected by copyright. All rights reserved.

Data Availability Statement

Research data are not shared.

Keywords

lithium–sulfur battery; iron dextran; H/Li–bond; cascade catalysis; lithium polysulfide conversion

Received: ((will be filled in by the editorial staff))

Revised: ((will be filled in by the editorial staff))

Published online: ((will be filled in by the editorial staff))

References

- [1] a) H. Chu, H. Noh, Y.-J. Kim, S. Yuk, J.-H. Lee, J. Lee, H. Kwack, Y. Kim, D.-K. Yang, H.-T. Kim, *Nat. Commun.* **2019**, *10*, 188; b) M. Zhao, X.-Y. Li, X. Chen, B.-Q. Li, S. Kaskel, Q. Zhang, J.-Q. Huang, *eScience*. **2021**, *1*, 44; c) N.-S. Choi, Z. Chen, S. A. Freunberger, X. Ji, Y.-K. Sun, K. Amine, G. Yushin, L. F. Nazar, J. Cho, P. G. Bruce, *Angew. Chem. Int. Ed.* **2012**, *51*, 9994
- [2] a) G. Li, S. Wang, Y. Zhang, M. Li, Z. Chen, J. Lu, *Adv. Mater.* **2018**, *30*, 1705590; b) X. Tao, J. Wang, C. Liu, H. Wang, H. Yao, G. Zheng, Z. W. Seh, Q. Cai, W. Li, G. Zhou, C. Zu, Y. Cui, *Nat. Commun.* **2016**, *7*, 11203; c) Y. Yang, G. Zheng, S. Misra, J. Nelson, M. F. Toney, Y. Cui, *J. Am. Chem. Soc.* **2012**, *134*, 15387
- [3] a) H. Wang, Y. Yang, Y. Liang, J. T. Robinson, Y. Li, A. Jackson, Y. Cui, H. Dai, *Nano Lett.* **2011**, *11*, 2644; b) N. Li, M. Zheng, H. Lu, Z. Hu, C. Shen, X. Chang, G. Ji, J. Cao, Y. Shi, *Chem. Commun.* **2012**, *48*, 4106; c) J. Guo, Y. Xu, C. Wang, *Nano Lett.* **2011**, *11*, 4288; d) S. Wei, H. Zhang, Y. Huang, W. Wang, Y. Xia, Z. Yu, *Energy Environ. Sci.* **2011**, *4*, 736; e) G. Xu, B. Ding, L. Shen, P. Nie, J. Han, X. Zhang, *J. Mater. Chem. A* **2013**, *1*, 4490; f) J. Wang, G. Li, D. Luo, Y.

This article is protected by copyright. All rights reserved.

- Zhang, Y. Zhao, G. Zhou, L. Shui, X. Wang, Z. Chen, *Adv. Energy Mater.* **2020**, *10*, 2002076; g) G. Xu, B. Ding, L. Shen, P. Nie, J. Han, X. zhang, *J. Mater. Chem. A* **2013**, *1*, 4490; h) H. Jiang, X.-C. Liu, Y. Wu, Y. Shu, X. Gong, F.-S. Ke, H. Deng, *Angew. Chem.* **2018**, *130*, 3980.
- [4] a) D. Liu, C. Zhang, G. Zhou, W. Lv, G. Ling, L. Zhi, Q.-H. Yang, *Adv. Sci.* **2018**, *5*, 1700270; b) J. Li, Z. Niu, C. Guo, M. Li, W. Bao, *J. Energy Chem.* **2021**, *54*, 434; c) X. Zhang, K. Chen, Z. Sun, G. Hu, R. Xiao, H.-M. Cheng, F. Li, *Energy Environ. Sci.* **2020**, *13*, 1076.
- [5] a) W. Liu, C. Luo, S. Zhang, B. Zhang, J. Ma, X. Wang, W. Liu, Z. Li, Q.-H. Yang, W. Lv, *ACS Nano* **2021**, *15*, 7491; b) M. Zhang, W. Chen, L. Xue, Y. Jiao, T. Lei, J. Chu, J. Huang, C. Gong, C. Yan, Y. Yan, Y. Hu, X. Wang, J. Xiong, *Adv. Energy Mater.* **2020**, *10*, 1903008.
- [6] a) X.-Q. Zhang, S. Feng, M. Zhao, C.-X. Zhao, X. Chen, B.-Q. Li, J.-Q. Huang, Q. Zhang, *Angew. Chem. Int. Ed.* **2022**, *61*, e202114671; b) X.-Q. Zhang, Q. Jin, Y.-L. Nan, L.-P. Hou, B.-Q. Li, X. Chen, Z.-H. Jin, X.-T. Zhang, J.-Q. Huang, Q. Zhang, *Angew. Chem. Int. Ed.* **2021**, *60*, 15503; c) M. Forsyth, H. Yoon, F. Chen, H. Zhu, D. R. MacFarlane, M. Armand, P. C. Howlett, *J. Phys. Chem. C* **2016**, *120*, 4276.
- [7] Z. Li, H. Jiang, N.-C. Lai, T. Zhao, Y.-C. Lu, *Chem. Mater.* **2019**, *31*, 10186.
- [8] a) K.-L. Hong, L. Qie, R. Zeng, Z.-Q. Yi, W. Zhang, D. Wang, W. Yin, C. Wu, Q.-J. Fan, W.-X. Zhang, Y.-H. Huang, *J. Mater. Chem. A* **2014**, *2*, 12733; b) Z. Wang, H. Wang, S. Qi, D. Wu, J. Huang, X. Li, C. Wang, J. Ma, *EcoMat* **2022**, *4*, e12200.
- [9] a) D. Dong, J. Xie, Z. Liang, Y.-C. Lu, *ACS Energy Lett.* **2022**, *7*, 123; b) Z. Huang, T. Wang, X. Li, H. Cui, G. Liang, Q. Yang, Z. Chen, A. Chen, Y. Guo, J. Fan, C. Zhi, *Adv. Mater.* **2022**, *34*, 2106180; c) J. Xie, Z. Liang, Y.-C. Lu, *Nat. Mater.* **2020**, *19*, 1006.

- [10] a) M. Zhao, X. Chen, X.-Y. Li, B.-Q. Li, J.-Q. Huang. *Adv. Mater.* **2021**, *33*, 2007298; b) B.-J. Lee, C. Zhao, J.-H. Yu, T.-H. Kang, H.-Y. Park, J. Kang, Y. Jung, X. Liu, T. Li, W. Xu, X.-B. Zuo, G.-L. Xu, K. Amine, J.-S. Yu. *Nat. Commun.* **2022**, *13*, 4629.
- [11] a) A. R. Elliott, A. S. Kizhakke Puliyakote, V. Tedjasaputra, B. Pazár, H. Wagner, R. C. Sá, J. E. Orr, G. Kim Prisk, P. D. Wagner, S. R. Hopkins, *Physiol Rep.* **2020**, *8*, e14488; b) W.-H. Ryu, F. S. Gittleson, J. M. Thomsen, J. Li, M. J. Schwab, G. W. Brudvig, A. D. Taylor, *Nat. Commun.* **2016**, *7*, 12925.
- [12] a) B. Sturm, H. Laggner, N. Ternes, H. Goldenberg, B. Scheiber-Mojdehkar, *Kidney Int.* **2005**, *67*, 1161; b) K. Chen, J. Suh, A. C. Carr, J. D. Morrow, J. Zeind, B. Frei, *Am. J. Physiol. Endocrinol. Metab.* **2000**, *279*, E1406.
- [13] a) M. Yang, T. Yan, M. Yu, J. Kang, R. Gao, P. Wang, Y. Zhang, H. Zhang, L. Shi, *Food Frontiers.* **2020**, *1*, 398; b) Y. Wang, Q. Li, L.-C. Zhang, Y. Wu, H. Chen, T. Li, M. Xu, S.-J. Bao, *J. Mater. Chem. A* **2021**, *9*, 7137.
- [14] Y. Dong, D. Cai, T. Li, S. Yang, X. Zhou, Y. Ge, H. Tang, H. Nie, Z. Yang, *ACS Nano* **2022**, *16*, 6414.
- [15] Y. Cheng, J. Shu, L. Xu, Y. Xia, L. Du, G. Zhang, L. Mai, *Adv. Energy Mater.* **2021**, *11*, 2100026.
- [16] a) S. Banerjee, S. Mukherjee, A. LaminKa-ot, S. R. Joshi, T. Mandal, G. Halder, *J. Adv. Res.* **2016**, *7*, 597; b) W. Chen, C. Zou, X. Li, L. Li, *RSC. Adv.* **2016**, *6*, 90682.
- [17] W. B. Fortune, M. G. Mellon, *Ind. Eng. Chem.* **1938**, *10*, 60.
- [18] a) Z. Huang, B. Song, H. Zhang, F. Feng, W. Zhang, K. Lu, Q. Chen, *Adv. Funct. Mater.* **2021**, *31*, 2100666; b) Y. Li, X. Lei, Y. Yuan, S. Wu, B. Han, X. Liu, W. Liu, J. Hu, C. Yang, Z. Lin, J. Lu, *ACS. Cent. Sci.* **2020**, *6*, 1827.
- [19] X. Zheng, L. Zhang, Z. Fan, Y. Cao, L. Shen, C. Au, L. Jiang, *Chem. Eng. J.* **2019**, *374*, 793.

- [20] C. Guo, M. Liu, G.-K. Gao, X. Tian, J. Zhou, L.-Z. Dong, Q. Li, Y. Chen, S.-L. Li, Y.-Q. Lan, *Angew. Chem. Int. Ed.* **2022**, *61*, e202113315.
- [21] a) C. Jiang, Q. Jia, M. Tang, K. Fan, Y. Chen, M. Sun, S. Xu, Y. Wu, C. Zhang, J. Ma, C. Wang, W. Hu, *Angew. Chem. Int. Ed.* **2021**, *60*, 10871; b) W. Zhang, Q. Wu, J. Huang, L. Fan, Z. Shen, Y. He, Q. Feng, G. Zhu, Y. Lu, *Adv. Mater.* **2020**, *32*, 2001740.
- [22] Y. Lai, H. Nie, X. Xu, G. Fang, X. Ding, D. Chan, S. Zhou, Y. Zhang, X. Chen, Z. Yang, *ACS Appl. Mater. Inter.* **2019**, *11*, 29978.
- [23] Z. Qiao, Y. Zhang, Z. Meng, Q. Xie, L. Lin, H. Zheng, B. Sa, J. Lin, L. Wang, D.-L. Peng, *Adv. Funct. Mater.* **2021**, *31*, 2100970.
- [24] Y. Huang, D. Lv, Z. Zhang, Y. Ding, F. Lai, Q. Wu, H. Wang, Q. Li, Y. Cai, Z. Ma, *Chem. Eng. J.* **2020**, *387*, 124122.
- [25] S. Zhou, S. Yang, D. Cai, C. Liang, S. Yu, Y. Hu, H. Nie, Z. Yang, *Adv. Sci.* **2022**, *9*, 2104205.
- [26] a) W. Wang, Z. Cao, G. A. Elia, Y. Wu, W. Wahyudi, E. Abou-Hamad, A.-H. Emwas, L. Cavallo, L.-J. Li, J. Ming, *ACS Energy Lett.* **2018**, *3*, 2899; b) X. Chen, Y.-K. Bai, C.-Z. Zhao, X. Shen, Q. Zhang, *Angew. Chem. Int. Ed.* **2020**, *59*, 11192.
- [27] L. Carbone, T. Coneglian, M. Gobet, S. Munoz, M. Devany, S. Greenbaum, J. Hassoun, *J. Power Sources* **2018**, *377*, 26.
- [28] H. Zhang, L. K. Ono, G. Tong, Y. Liu, Y. Qi, *Nat. Commun.* **2021**, *12*, 4738.
- [29] R. Wang, C. Luo, T. Wang, G. Zhou, Y. Deng, Y. He, Q. Zhang, F. kang, W. Lv, Q.-H. Yang, *Adv. Mater.* **2020**, *32*, 2000315.
- [30] D. W. Dees, S. Kawauchi, D. P. Abraham, J. Prakash, *J. Power Sources* **2009**, *189*, 263.

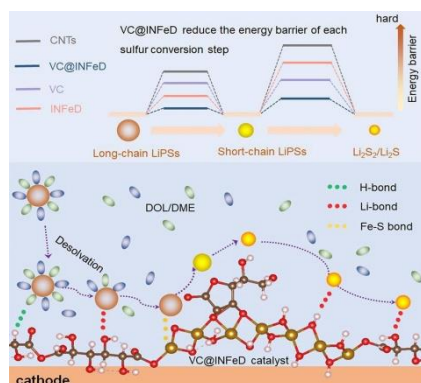
- [31] a) D. Cai, B. Liu, D. Zhu, D. Chen, M. Lu, J. Cao, Y. Wang, W. Huang, Y. Shao, H. Tu, W. Han, *Adv. Energy Mater.* **2020**, *10*, 1904273; b) E. Ghasemiestahbanati, A. Shehzad, K. Konstas, C. J. Setter, L. A. O'Dell, M. Shaibani, M. Majumder, M. R. Hill, *J. Mater. Chem. A* **2022**, *10*, 902.
- [32] B. Zhang, C. Luo, G. Zhou, Z.-Z. Pan, J. Ma, H. Nishihara, Y.-B. He, F. Kang, W. Lv, Q.-H. Yang, *Adv. Funct. Mater.* **2021**, *31*, 2100793.
- [33] B. Wang, L. Wang, B. Zhang, S. Zeng, F. Tian, J. Dou, Y. Qian, L. Xu, *ACS Nano* **2022**, *16*, 4947.
- [34] F. Ma, Y. Wan, X. Wang, X. Wang, J. Liang, Z. Miao, T. Wang, C. Ma, G. Lu, J. Han, Y. Huang, Q. Li, *ACS Nano* **2020**, *14*, 10115.
- [35] C.-X. Zhao, X.-Y. Li, M. Zhao, Z.-X. Chen, Y.-W. Song, W.-J. Chen, J.-N. Liu, B. Wang, X.-Q. Zhang, C.-M. Chen, B.-Q. Li, J.-Q. Huang, Q. Zhang, *J. Am. Chem. Soc.* **2021**, *143*, 19865.
- [36] L. Zhang, P. Liang, X.-L. Man, D. Wang, J. Huang, H.-B. Shu, Z.-G. Liu, L. Wang, *J. Phys. Chem. Solids* **2019**, *126*, 280.
- [37] a) L. Peng, Z. Wei, C. Wan, J. Li, Z. Chen, D. Zhu, D. Baumann, H. Liu, C. S. Allen, X. Xu, A. I. Kirkland, I. Shakir, Z. Almutairi, S. Tolbert, B. Dunn, Y. Huang, P. Sautet, X. Duan, *Nat. Catal.* **2020**, *3*, 762; b) Z. Wang, H. Ji, L. Zhou, X. Shen, L. Gao, J. Liu, T. Yang, T. Qian, C. Yan, *ACS Nano* **2021**, *15*, 13847.

Table of Content

Desolvation Synergy of Multiple H/Li-bonds on Iron-Dextran-based Catalyst Stimulates Lithium-Sulfur Cascade Catalysis

This article is protected by copyright. All rights reserved.

Tingting Li, Dong Cai*, Shuo Yang*, Yangyang Dong, Shuang Yu, Ce Liang, Xuemei Zhou, Yongjie Ge, Kuikui Xiao, Huagui Nie, Zhi Yang*



In this work, we developed a highly efficient VC@INFeD catalyst in lithium-sulfur batteries, accomplishing fast de-solvation and enrichment of high-concentration LIPs by multiple H/Li-bonds and resolving subsequent sulfur transformations through cascade catalytic sites where INFeD and VC promote the conversions of long-chain and short-chain LiPSs, respectively, which substantially reduce energy barriers and eliminate LiPS shuttling effects.

This article is protected by copyright. All rights reserved.